Article

Not peer-reviewed version

Chiral Jahn-Teller Distortion in Quasi-Planar Boron Clusters

Dongbo Zhao *, Xin He, Yilin Zhao, Tianlv Xu, Shankai Hu, Paul W. Ayers *, Shubin Liu *

Posted Date: 14 February 2024

doi: 10.20944/preprints202402.0801.v1

Keywords: Jahn-Teller effect; Helical spin density; Helical molecular orbital; Boron clusters

Article

Chiral Jahn-Teller Distortion in Quasi-Planar Boron Clusters

Dongbo Zhao [1,*], Yilin Zhao [2], Tianlv Xu [3], Xin He [4], Shankai Hu [1], Paul W. Ayers [2,*] and Shubin Liu [5,6,*]

[1] Institute of Biomedical Research, Yunnan University, Kunming 650500, Yunnan, China
[2] Department of Chemistry and Chemical Biology, McMaster University, Hamilton, ONL8S 4M1, Canada
[3] College of Chemistry and Chemical Engineering, Hunan Normal University, Changsha, Hunan 410081, China
[4] Qingdao Institute for Theoretical and Computational Sciences, Shandong University, Qingdao 266237, China
[5] Research Computing Center, University of North Carolina, Chapel Hill, North Carolina 27599-3420, USA
[6] Department of Chemistry, University of North Carolina, Chapel Hill, North Carolina 27599-3290, USA
* Correspondence: dongbo@ynu.edu.cn (D.Z.); ayers@mcmaster.ca (P.W.A.); shubin@email.unc.edu (S.L.)

Abstract: Helical (frontier) molecular orbitals [*Chem. Sci.* **2013**, *4*, 4278] were reported a decade ago, but helical molecular spin densities [*Mol. Phys.* **2022**, e2157774] have been observed by us only very recently. In this work, we have observed that some chiral boron clusters (B_{16}^-, B_{20}^-, B_{24}^-, and B_{28}^-) can simultaneously have helical molecular orbitals and helical spin densities; these seem to be the first compounds discovered to have this intriguing property. We show that chiral Jahn-Teller distortion of quasi-planar boron clusters drives the formation of the helical molecular spin densities in these clusters and show that elongation/enhancement of helical molecular orbitals can be achieved by simply adding more building blocks via a linker. Aromaticity of these boron clusters is discussed. Chiral boron clusters may find potential applications in spintronics, such as molecular magnets.

Keywords: jahn-teller effect; helical spin density; helical molecular orbital; boron clusters

1. Introduction

While they are not experimental observables, molecular orbitals are conceptually useful and elegant tool for elucidating molecular properties [1]. They have long been a significant tool in the arsenal of chemists [2–6], tracing back to the early work of Hückel, Mulliken, and others. One prominent example is the principle of conservation of orbital symmetry [7–9], which subsumes the Woodward-Hoffmann rules. Helical frontier molecular orbitals, first introduced by Hendon et al. [10] in 2013, have seeded a surge of interest. Helical frontier molecular orbitals appear in disubstituted allenes and even-*n* cumulenes. Later, many more types of molecules possessing this interesting property were reported [11–29], and it was discovered that molecules with helical orbitals have interesting physicochemical properties. For example, oligoyne-bridged bifluorenes can induce spin–orbit coupling [29].

Boron forms clusters with unique bonding, aromaticity, and reactivity properties [30–32]. Very recently [33], we have observed helical spin densities of anionic boron clusters. In this work, we report that B_{16}^- [34], B_{20}^- [35], B_{24}^- [36], and B_{28}^- [37] (see **Scheme 1**) not only have helical molecular orbitals, but also helical spin densities. This is interesting because, unlike molecular orbitals, spin-densities are experimental observables, and this allows the edifice of (spin)-resolved (conceptual) density-functional theory [38–49] to be directly applied to these compounds.

To pin down the origin of spin-density helicity, we forced the quasi-planar boron atoms to be exactly in a plane: helical spin densities are no longer observed. Thus, it is chiral Jahn-Teller distortion that governs the formation of helical spin densities. This seems to be the first observation of this intriguing phenomenon in inorganic boron clusters. We also show that elongation or enlargement of

Preprints.org (www.preprints.org) | NOT PEER-REVIEWED | Posted: 14 February 2024 doi:10.20944/preprints202402.0801.v1

helical molecular orbitals can be achieved by simply adding more structural motifs via a linker. Moreover, we have exhibited that helical-shape molecules have a large propensity to assume helical molecular orbitals as shown in inorganic species P_9^+ [50], $Be_6B_{11}^-$ [51], and As_{11}^{3-} [52] (*vide infra*).

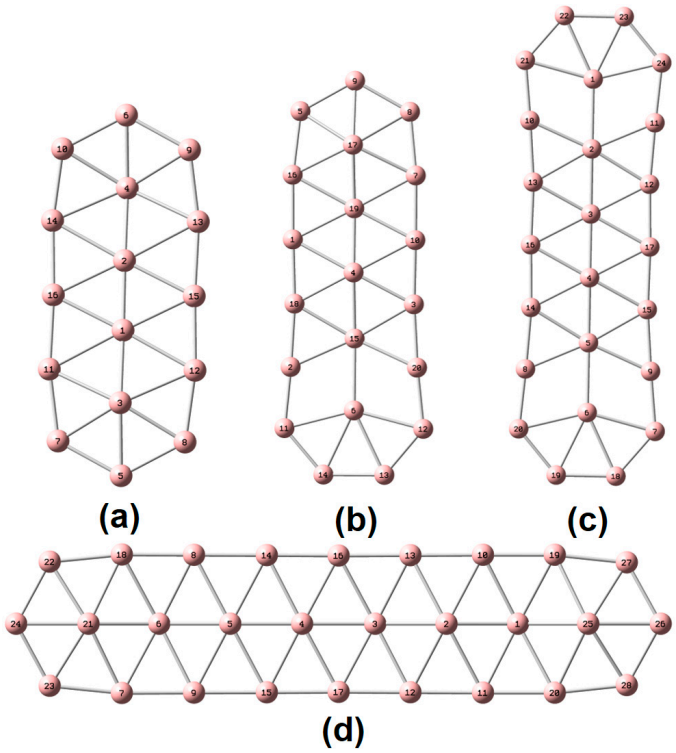

Scheme 1. Molecular representation of (a) B_{16}^-, (b) B_{20}^- (c) B_{24}^-, and (d) B_{28}^- and the corresponding atomic numberings.

2. Results

To characterize the planarity of anionic boron clusters (in both the ground- and excited-state), we used a few parameters [53], including molecular planarity parameter (MPP), span of deviation from plane (SDP), maximum positive/negative deviation (MPD/MND) to the fitted plane, as listed in **Table 1**. The fitted parameters of a plane are listed in **Table S1**. One can easily discover that all the systems studied in this work are quasi-planar. Based upon the optimized structures in the ground state, we have observed helical spin densities as exhibited in **Figure 1**. No similar results are discerned for the excited-state structures (see **Figure S1**).

Table 1. Molecular planarity parameter (MPP), span of deviation from plane (SDP), maximum positive/negative deviation (MPD/MND) to the fitted plane[a].

species	MPP	SDP	MPD	MND
$^2B_{16}^-$	0.090	0.442	0.221	–0.221
$^4B_{16}^-$	0.017	0.091	0.047	–0.044
$^2B_{20}^-$	0.081	0.382	0.263	–0.119
$^4B_{20}^-$	0.083	0.322	0.179	–0.143
$^2B_{24}^-$	0.021	0.074	0.037	–0.037
$^4B_{24}^-$	0.039	0.196	0.098	–0.098
$^2B_{28}^-$	0.092	0.440	0.302	–0.138
$^4B_{28}^-$	0.103	0.404	0.212	–0.192

[a] Units are in Å.

 doi:10.20944/preprints202402.0801.v1

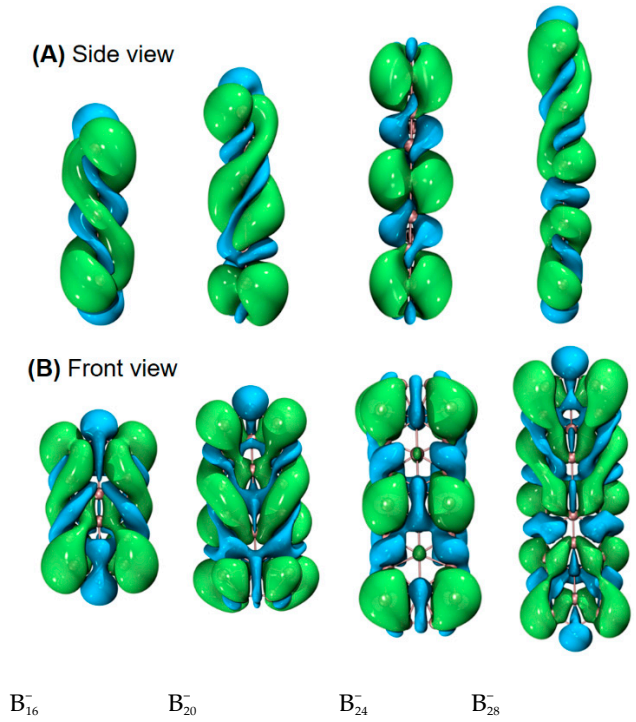

Figure 1. Helical spin densities of quasi-planar boron clusters B_{16}^-, B_{20}^-, B_{24}^-, and B_{28}^- obtained at the PBE0/6-311+G(d) level from both (A) side and (B) front views. The isovalue was set to be 0.0004 a.u. Molecular renderings were achieved via the VMD [54] software.

To elucidate the origin of helical spin densities, we force the ground-state quasi-planar boron structures to be exactly planar followed by single-point calculations at the PBE0/6-311+G(d) [55,56] level. The spin-densities' helicity then vanishes (see **Figure S2**). Accordingly, a chiral Jahn-Teller distortion plays a key role where the right- and left-handed deformations are (quasi)equal in energy, and the planar structure deforms slightly to break symmetry, thus lowering in energy. More intriguingly, these chiral structures [in terms of vibrational circular dichroism (VCD) spectra, see **Figure 2** for details] can also have helical frontier molecular orbitals as shown in **Figure 3**. Of note, excited-state VCD spectra are also observed as shown in **Figure S3**. In the ground state, except for B_{24}^-, B_{16}^-, B_{20}^-, and B_{28}^- indeed have helical β–LUMOs (with lower orbital energies than their α counterparts) and B_{16}^- and B_{20}^- also have β–HOMOs in **Figure 3**; in the excited state, only B_{20}^-, and B_{28}^- have helical β–HOMOs.

Preprints.org (www.preprints.org) | NOT PEER-REVIEWED | Posted: 14 February 2024 doi:10.20944/preprints202402.0801.v1

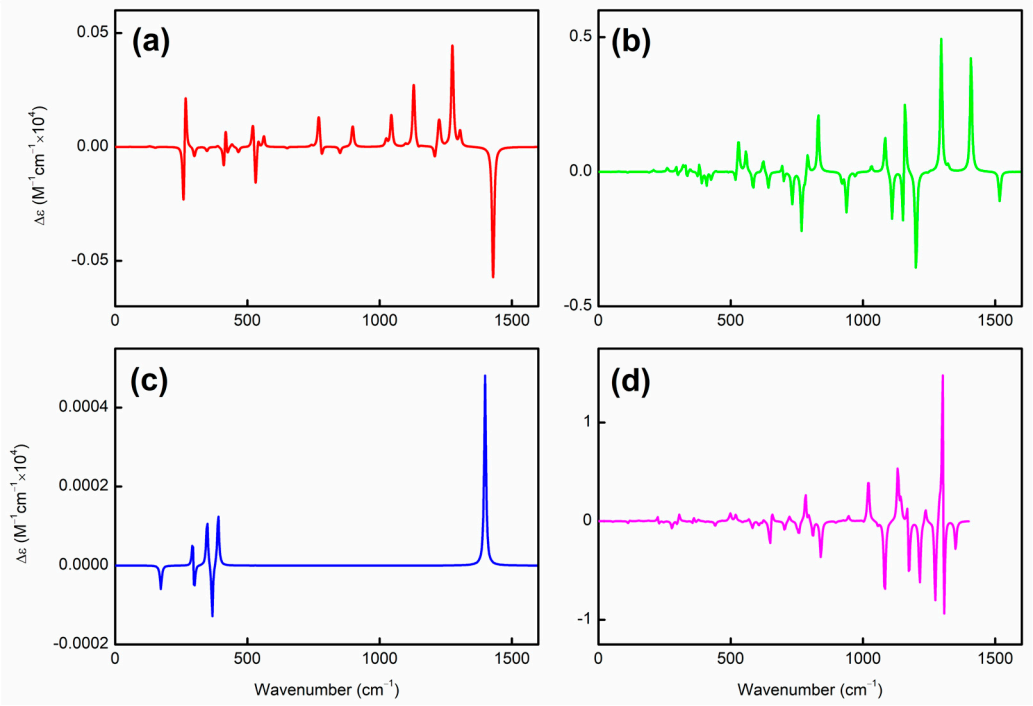

Figure 2. VCD spectra of (a) B_{16}^-, (b) B_{20}^-, (c) B_{24}^-, and (d) B_{28}^- obtained at the PBE0/6-311+G(d) level. The *x*/*y*-axis spans from (a) to (d).

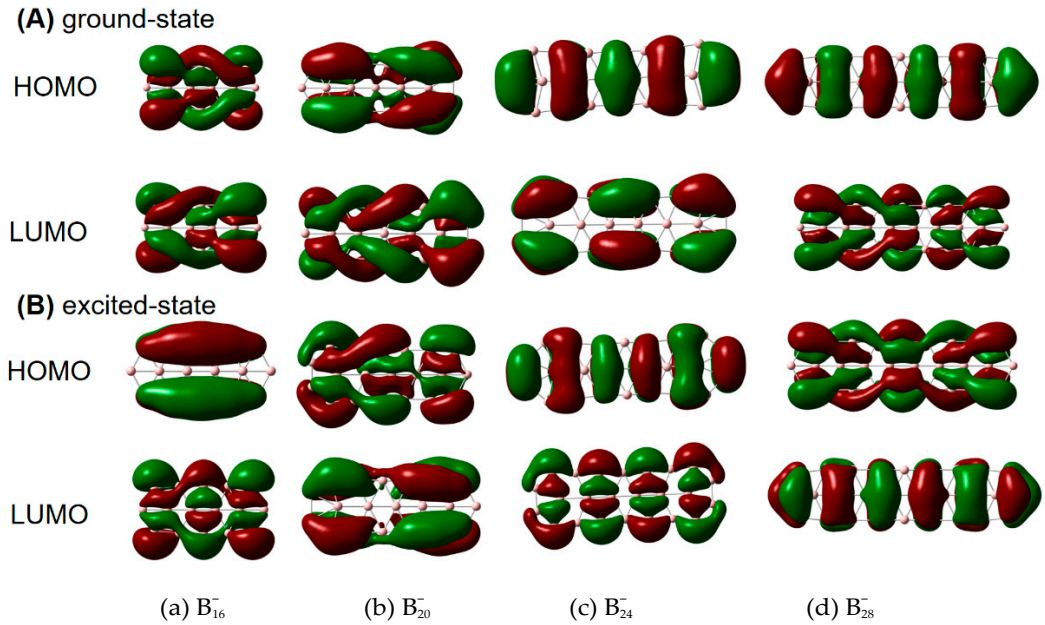

Figure 3. *β*–HOMOs and *β*–LUMOs of (A) ground- and (B) excited-state B_{16}^-, B_{20}^-, B_{24}^-, and B_{28}^- obtained at the PBE0/6-311+G(d) level from both side and front views. The isovalue was set to be 0.02 a.u. Molecular renderings were achieved via the GaussView6.0 [57] software.

Figure 4 shows the GIMIC (gauge-including magnetically induced current) [59,60] distributions of both ground- and excited-state B_{16}^-, B_{20}^-, B_{24}^-, and B_{28}^-. For $^2B_{16}^-$ and $^4B_{16}^-$, the induced electric currents are running counter-clockwise, which is indicative of aromaticity, as evidenced by the negative NICS (nucleus-independent chemical shift) [61] values in **Table 2**. Similar results are observed for B_{24}^- and B_{28}^-. However, this is not the case for B_{20}^-. The overall effect indicates that B_{20}^- is antiaromatic while the *Z*-component of the induced electric current also runs in a counter-clockwise manner as showcased

Preprints.org (www.preprints.org) | NOT PEER-REVIEWED | Posted: 14 February 2024 doi:10.20944/preprints202402.0801.v1

by the NICSzz values in **Table 2**. Yet, the dominant contributions of the induced electric current lie in the x-y plane which is the source of antiaromaticity. To go a step further, **Figure 5** showcases the 3D isotropic shielding surface (ICSS) [62] calculations for both ground- and excited-state boron clusters and it is clearly revealed that there exist strongly shielded chemical environment along the direction perpendicular to the quasi-planar boron clusters.

Table 2. Ground- and excited-state aromaticity of B_{16}^-, B_{20}^-, B_{24}^-, and B_{28}^- in terms of the global NICS values[a].

species	NICS(0)	NICS(0)zz	NICS(1)	NICS(1)zz	NICS(–1)	NICS(–1)zz
$^2B_{16}^-$	–16.67	–48.74	–17.90	–39.52	–17.90	–39.52
$^4B_{16}^-$	–16.76	–111.92	–5.85	–4.66	–5.83	–4.66
$^2B_{20}^-$	15.51	–28.62	–15.89	–31.60	–11.26	–23.02
$^4B_{20}^-$	22.94	–15.48	–13.61	–32.13	–13.57	–30.98
$^2B_{24}^-$	–29.53	–47.96	–14.42	–26.37	–14.42	–26.37
$^4B_{24}^-$	–26.90	–59.08	–16.85	–38.44	–16.85	–38.44
$^2B_{28}^-$	–18.76	–33.63	–8.27	–16.35	–8.87	–15.98
$^4B_{28}^-$	–17.24	–36.36	–11.94	–22.62	–11.74	–23.33

[a] PBE0/pcJ-2. Units are in ppm. NICS(0) corresponds to the NICS value at the global center, NICS(1) at point 1 Å above the global center, and NICS(–1) at point 1.0 Å below the global center. The z-axis component is denoted as NICSzz.

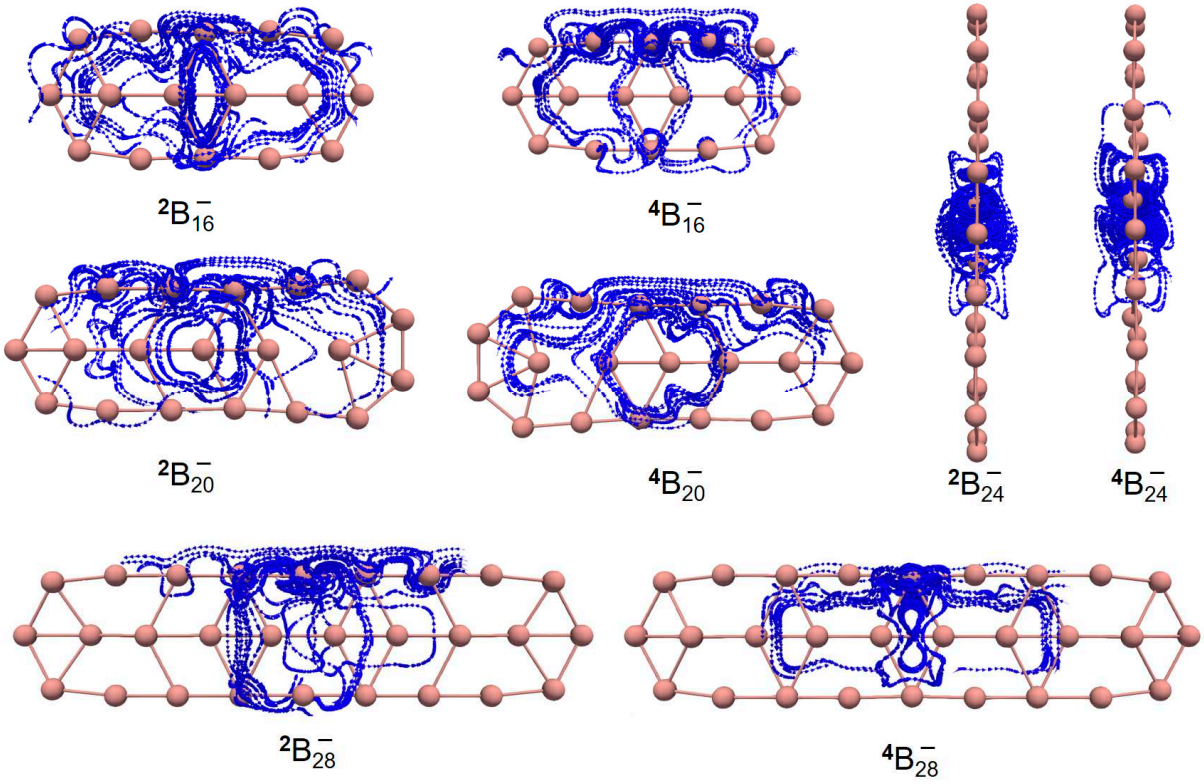

Figure 4. The GIMIC diagrams of both ground- and excited-state of B_{16}^-, B_{20}^-, B_{24}^-, and B_{28}^-. Molecular renderings were achieved via the ParaView [58] software.

Preprints.org (www.preprints.org) | NOT PEER-REVIEWED | Posted: 14 February 2024 doi:10.20944/preprints202402.0801.v1

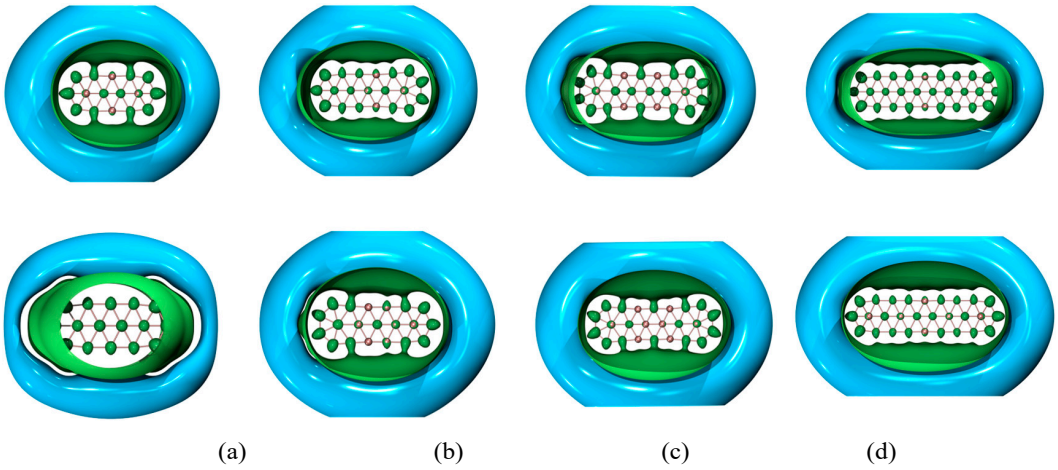

Figure 5. 3D ICSS maps of both ground- (upper panel) and excited-state (lower panel) (a) B_{16}^-, (b) B_{20}^-, (c) B_{24}^-, and (d) B_{28}^-. The isovalue was set to be 0.02 a.u. The inner green surface is positive and outer cyan surface is negative. Molecular renderings were achieved via the VMD [54] software.

Hyperfine coupling constants [63,64] provide a direct experimental measure of the distribution of unpaired spin density in paramagnetic molecules. The interactions of unpaired electrons with external magnetic fields arise from the Zeeman effect and from the hyperfine coupling with nuclei having nonzero spins. The latter contribution is related to the chemical environment. For each nucleus N of a molecule located at $\mathbf{r}_N$, the isotropic component of the hyperfine interaction tensor, $a(N)$, is related to the local spin density through [65]

$$a(N) = \frac{8\pi}{3}\beta_e\beta_N g_N \sum_{\mu\nu} \mathbf{P}_{\mu\nu}^{\alpha-\beta}\langle\varphi_\mu|\delta(\mathbf{r}-\mathbf{r}_N)|\varphi_\nu\rangle$$

where β_e, β_N, and g_N are the electronic and nuclear magnetons and the nuclear magnetogiric ratio, the indices μ and ν run over the basis functions, $\mathbf{P}_{\mu\nu}^{\alpha-\beta}$ is the difference between the density matrices of spin α and spin β electrons and $\delta(\mathbf{r}-\mathbf{r}_N)$ is the Dirac delta function. Therefore, once the density matrices for different spins have been determined the calculation of $a(N)$ for each nucleus is achieved in a straightforward way. The (isotropic) hyperfine coupling tensor, $\mathbf{A}_{\mathrm{iso}}^N$, consists of the Fermi contact term ($\mathbf{A}_{\mathrm{FC}}^N$) and a spin orbit correction, the pseudocontact term ($\mathbf{A}_{\mathrm{PC}}^N$).

Shown in **Table 3** are the isotropic NMR shielding (α_{iso}) constants and hyperfine coupling ($\mathbf{A}_{\mathrm{iso}}$) constants for both ground- and excited-state B_{16}^- at the PBE0/pcJ-2 [66,67] level. It is clearly shown that the 16 boron atoms can be roughly grouped into 5 different atoms in different chemical environments as evidenced both by the α_{iso} and $\mathbf{A}_{\mathrm{iso}}$ data. Among all the boron atoms, one can easily see that atoms 5 and 6 (as shown in **Scheme 1**), lying at the two ends of the middle line composed of atoms 1 – 6, are the most unique. For example, they have the least positive α_{iso} values and the most negative $\mathbf{A}_{\mathrm{iso}}$ data. In addition, they undergo the largest changes when going from the ground state to the excited state. Specifically, $\mathbf{A}_{\mathrm{iso}}$ changes by ~18 MHz while the largest change of the other atoms is ~8 MHz. Similar trends can be observed for B_{20}^-, B_{24}^-, and B_{28}^- as shown in **Tables 4–6**.

Table 3. Isotropic NMR shielding constants (α_{iso}, in ppm) and Fermi contact couplings ($\mathbf{A}_{\mathrm{iso}}$, in MHz) for ground-state (columns 2, 3, 7, and 8) and excited-state (columns 4, 5, 9, and 10) B_{16}^-.

no	$^2\alpha_{\mathrm{iso}}$	$^2\mathbf{A}_{\mathrm{iso}}$	$^4\alpha_{\mathrm{iso}}$	$^4\mathbf{A}_{\mathrm{iso}}$	no	$^2\alpha_{\mathrm{iso}}$	$^2\mathbf{A}_{\mathrm{iso}}$	$^4\alpha_{\mathrm{iso}}$	$^4\mathbf{A}_{\mathrm{iso}}$
1	77.66	–2.98	78.50	–1.53	9	35.33	40.64	25.78	32.87
2	77.66	–2.98	78.50	–1.56	10	35.34	40.58	25.78	32.86
3	81.47	–5.77	72.32	–8.74	11	69.43	–11.44	82.41	–10.30
4	81.47	–5.77	72.33	–8.74	12	69.42	–11.46	82.41	–10.30
5	8.77	–35.62	36.11	–17.18	13	69.43	–11.44	82.41	–10.30
6	8.77	–35.62	36.11	–17.19	14	69.43	–11.46	82.41	–10.30
7	35.33	40.66	25.78	32.86	15	102.86	–3.11	78.37	0.72

 doi:10.20944/preprints202402.0801.v1

8	35.34	40.60	25.78	32.85	16	102.86	–3.10	78.37	0.72

Table 4. Isotropic NMR shielding constants (α_{iso}, in ppm) and Fermi contact couplings ($\mathbf{A}_{iso}$, in MHz) for ground-state (columns 2, 3, 7, and 8) and excited-state (columns 4, 5, 9, and 10) B_{20}^-.

no	$^2\alpha_{iso}$	$^2\mathbf{A}_{iso}$	$^4\alpha_{iso}$	$^4\mathbf{A}_{iso}$	no	$^2\alpha_{iso}$	$^2\mathbf{A}_{iso}$	$^4\alpha_{iso}$	$^4\mathbf{A}_{iso}$
1	82.41	0.71	92.94	1.07	11	39.89	24.08	44.65	13.31
2	75.99	–17.57	64.17	–7.19	12	39.89	24.09	44.53	13.25
3	94.80	5.82	117.43	–0.87	13	26.91	–9.85	30.45	–7.18
4	82.47	–15.30	78.11	–12.48	14	26.91	–9.86	30.46	–7.30
5	18.41	35.48	38.64	35.92	15	78.73	2.80	92.78	2.47
6	78.05	–9.61	74.29	–9.04	16	81.60	–10.16	69.88	–8.16
7	81.60	–10.16	69.82	–8.20	17	69.79	–9.31	79.02	–7.43
8	18.42	35.48	38.84	35.95	18	94.79	5.81	117.62	–0.91
9	34.65	–21.98	19.20	–27.86	19	77.81	4.31	86.55	0.07
10	82.41	0.73	93.02	1.02	20	75.99	–17.58	64.29	–7.26

Table 5. Isotropic NMR shielding constants (α_{iso}, in ppm) and Fermi contact couplings ($\mathbf{A}_{iso}$, in MHz) for ground-state (columns 2, 3, 7, and 8) and excited-state (columns 4, 5, 9, and 10) B_{24}^-.

no	$^2\alpha_{iso}$	$^2\mathbf{A}_{iso}$	$^4\alpha_{iso}$	$^4\mathbf{A}_{iso}$	no	$^2\alpha_{iso}$	$^2\mathbf{A}_{iso}$	$^4\alpha_{iso}$	$^4\mathbf{A}_{iso}$
1	80.03	–5.46	79.50	–7.42	13	118.46	–9.58	120.01	–3.83
2	78.34	1.45	79.92	5.62	14	118.46	–9.58	120.01	–3.83
3	83.41	–5.35	88.96	–3.69	15	118.46	–9.58	120.01	–3.83
4	83.41	–5.35	88.96	–3.69	16	68.85	12.02	70.01	4.22
5	78.34	1.45	79.92	5.62	17	68.85	12.02	70.01	4.22
6	80.03	–5.46	79.50	–7.42	18	28.82	–8.41	17.95	–3.84
7	38.44	8.36	45.29	1.03	19	28.82	–8.41	17.95	–3.84
8	66.10	–7.13	64.54	–4.36	20	38.44	8.36	45.29	1.03
9	66.10	–7.13	64.54	–4.36	21	38.44	8.36	45.29	1.03
10	66.10	–7.13	64.54	–4.36	22	28.82	–8.41	17.95	–3.84
11	66.10	–7.13	64.54	–4.36	23	28.82	–8.41	17.95	–3.84
12	118.46	–9.58	120.01	–3.83	24	38.44	8.36	45.29	1.03

Table 6. Isotropic NMR shielding constants (α_{iso}, in ppm) and Fermi contact couplings ($\mathbf{A}_{iso}$, in MHz) for ground-state (columns 2, 3, 7, and 8) and excited-state (columns 4, 5, 9, and 10) B_{28}^-.

no	$^2\alpha_{iso}$	$^2\mathbf{A}_{iso}$	$^4\alpha_{iso}$	$^4\mathbf{A}_{iso}$	no	$^2\alpha_{iso}$	$^2\mathbf{A}_{iso}$	$^4\alpha_{iso}$	$^4\mathbf{A}_{iso}$
1	79.30	–7.09	70.30	5.31	15	69.93	–19.78	84.30	0.54
2	73.04	–1.60	84.98	–5.58	16	96.89	31.15	98.54	–1.44
3	83.12	–5.16	78.07	–0.08	17	96.89	31.14	98.57	–1.44
4	84.30	–6.42	78.12	–0.08	18	78.19	–18.49	81.49	–5.32
5	76.95	–3.58	84.99	–5.61	19	74.86	–16.35	81.54	–5.27
6	79.95	–6.84	70.29	5.14	20	74.86	–16.35	81.52	–5.26
7	78.19	–18.49	81.52	–5.34	21	70.58	–4.58	75.02	–5.81
8	82.74	13.22	91.03	–1.62	22	17.52	50.44	29.89	11.67
9	82.74	13.22	90.88	–1.57	23	17.52	50.45	29.91	11.70
10	77.86	17.29	90.69	–1.61	24	37.06	–33.92	16.67	–9.92
11	77.87	17.30	90.80	–1.66	25	63.54	–0.51	74.89	–5.83
12	68.99	–21.28	84.21	0.63	26	42.21	–19.68	16.75	–9.76
13	68.99	–21.28	84.33	0.62	27	14.01	33.86	29.71	11.46
14	69.93	–19.77	84.19	0.55	28	14.00	33.88	29.66	11.45

 doi:10.20944/preprints202402.0801.v1

3. Discussion

Helical frontier molecular orbitals were reported first for hydrocarbon systems, then also for boron-containing molecules [10]. In this work, we have also observed similar results for quasi-planar boron clusters. In addition, as shown in **Figure 6**, for some other helical (inorganic) motifs, P_9^+, $Be_6B_{11}^-$ (a B_{11} helical structure plus a distorted prism of Be_6), and As_{11}^{3-}, helical frontier molecular orbitals are also observed. Is this helicity a ubiquitous phenomenon or a special feature of some elements in special molecular topologies? This seems to be an open question, and will be a topic for future research.

While a systematic rule for designing molecular templates with helical spin-densities is unknown to us, we can show how to elongate the helical frontier molecular orbitals from a given template structure. For example, starting from a conjugated hydrocarbon molecule **1** with helical frontier molecular orbitals, combining two monomers of **1** and a linker, such as $CH_2(\mathbf{1})_2$, $[NH_2(\mathbf{1})_2]^+$, and $[OH(\mathbf{1})_2]^+$, leads to elongated or enlarged helical frontier molecular orbitals as shown in **Figure 7**. Yet, when three or four monomers of **1** are grouped together, such as $CH(\mathbf{1})_3$ or $C(\mathbf{1})_4$, the helical frontier molecular orbitals are no longer elongated (results not shown). Is it possible to generate an infinite chain of $(\mathbf{1})_\infty$? We do not know; possibly other linkers would work better. For the anionic boron clusters, we failed to even generate a dimer of B_{16}^-; this is presumably because the repulsion between the anionic monomers prevents electron delocalization between them.

Finally, we have to point out that in a broader sense, dissection of chiral boron clusters and the electron spin should be beneficial to its applications to chiral spintronics and materials [68,69,70].

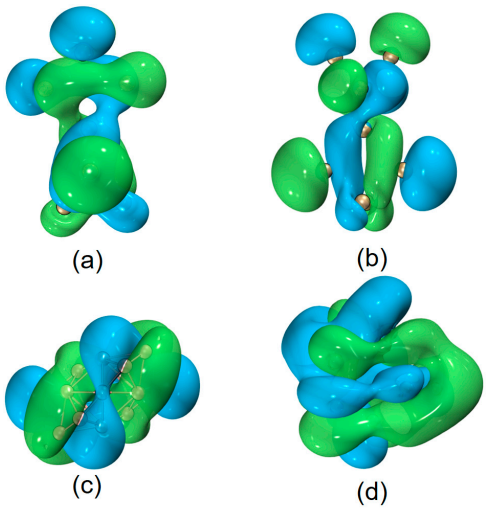

Figure 6. Helical HOMOs of [(a) and (b)] P_9^+, (c) $Be_6B_{11}^-$, and (d) As_{11}^{3-}, respectively. The isovalue was set to be 0.02 a.u. for P_9^+ and 0.01 a.u. for $Be_6B_{11}^-$ and As_{11}^{3-}. Molecular renderings were achieved via the VMD [54] software.

Preprints.org (www.preprints.org) | NOT PEER-REVIEWED | Posted: 14 February 2024 doi:10.20944/preprints202402.0801.v1

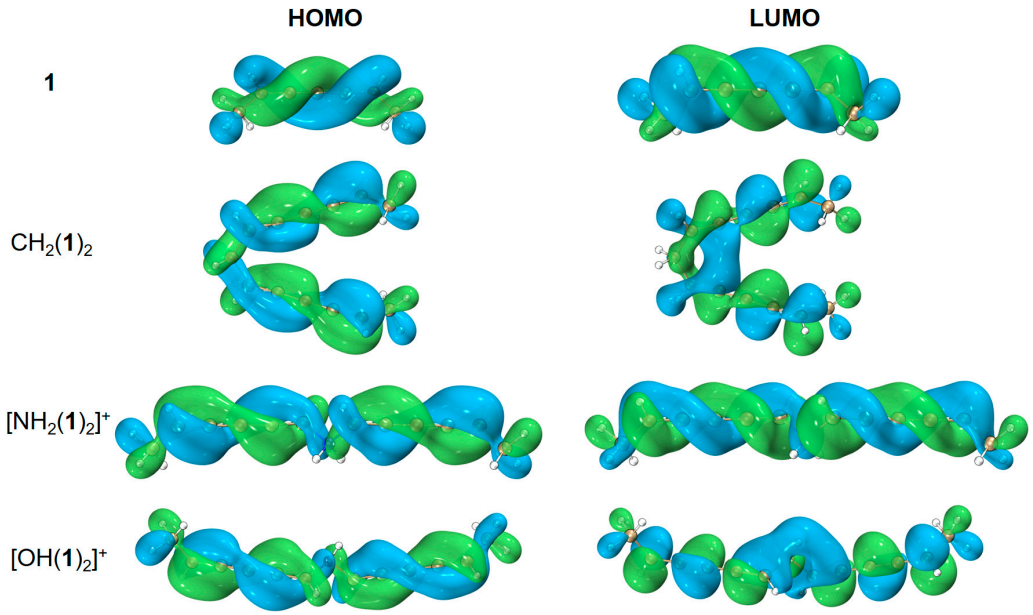

Figure 7. Elongation/enhancement of helical frontier molecular orbitals. The isovalue was set to be 0.02 a.u. Molecular renderings were achieved via the VMD [54] software. .

4. Materials and Methods

For molecular systems, structure optimization was performed at the density functional theory (DFT) [71,72] PBE0/6-311+G(d) level. Stability of molecular wavefunctions was confirmed via keywords of "guess=mix" and "stable=opt" in Gaussian 16 [73]. Vibrational frequency calculations were ensued to make sure that all the structures were true local minima on the potential energy surface. The optimized atomic Cartesian coordinates are supplied in the Supplementary Materials. Multireference (MR) characteristics of all boron clusters were checked via the T1 diagnostics [74] at the coupled cluster theory with single and double substitutions [CCSD/6-311+G(d)] and the frozen core formalism was used for CCSD calculations. The reported values are 0.036, 0.049, 0.034, and 0.041 for the ground state; 0.041, 0.041, 0.040, and 0.037 for the excited state, indicative of substantial multi-reference characteristics (because their T1 > 0.02). To further analyze the aromaticity properties of boron clusters, we employed PBE0/pcJ-2 to calculate the global NICS (nucleus-independent chemical shift) values and GIMIC (gauge-including magnetically induced current) distributions. NMR chemical shielding constants and isotropic hyperfine coupling parameters were obtained at the PBE0/pcJ-2 level with default gauge-including atomic orbitals (GIAOs) [75–79]. All DFT calculations were performed by using the Gaussian 16 package with tight self-consistent field (SCF) convergence criteria and ultrafine integration grids to ensure good accuracy. The Multiwfn [80] software was used to analyze the planarity of boron clusters and prepare the ICSS input files.

5. Summary

We have observed that helical molecular orbitals and helical spin densities can coexist in a chiral quasi-planar boron cluster. We show that this intriguing phenomenon emerges due to chiral Jahn-Teller distortion of planar boron clusters and show how to generate elongated or enhanced helical molecular orbitals by grouping a building blocks together via a linker. Finally, we found that helical inorganic species have a strong propensity to assume helical molecular orbitals. For potential applications in spintronics, it is interesting to study whether the observed helical spin densities would still be observed for boron clusters adsorbed on metal surfaces. Work along these lines is in progress.

Supplementary Materials: Optimized structures, excited-state VCD spectra, excited-state spin densities, fitted parameters of the planes of boron clusters, and the ground-state spin density maps of planar boron clusters. The

following supporting information can be downloaded at the website of this paper posted on Preprints.org., Figure S1: title; Table S1: title; Video S1: title.

Author Contributions: Conceptualization, S.L., P.W.A. and D.Z.; data curation, Y.Z. X.T. X.H. S.H. and D.Z.; formal analysis, Y.Z. X.T. X.H. S.H. and D.Z.; funding acquisition, P.W.A. and D.Z.; project administration, S.L. P.W.A. and D.Z.; supervision, S.L., P.W.A. and D.Z.; writing—original draft, D.Z.; writing—review and editing, S.L., P.W.A. and D.Z. All authors have read and agreed to the final version of the manuscript.

Funding: This work is supported by the National Natural Science Foundation of China (grant no. 22203071), the Yunnan Fundamental Research Projects (grant no. 202101AU070012), the start-up funding of Yunnan University, NSERC, Canada Research Chairs, and the Digital Research Alliance of Canada.

Institutional Review Board Statement: Not applicable.

Informed Consent Statement: Not applicable.

Data Availability Statement: Data is contained within the article.

Acknowledgments: Part of the computations were done on the high performance computers of the Advanced Computing Center of Yunnan University.

Conflicts of Interest: The authors declare no conflicts of interest.

References

1. Krylov, A.I. From orbitals to observables and back. *J. Chem. Phys.* **2020**, *153*, 080901.
2. Jin, Z.; Li, Y.; Hu, Z.; Hu, B.; Liu, Y.; Iida, K.; Kamazawa, K.; Stone, M.B.; Kolesnikov, A.I.; Abernathy, D.L.; Zhang, X.; Chen, H.; Wang, Y.; Fang, C.; Wu, B.; Zaliznyak, I.A.; Tranquada, J.M.; Li, Y. Magnetic molecular orbitals in MnSi. *Sci. Adv.* **2023**, *9*, eadd5239.
3. Mazin, I.I.; Jeschke, H.O.; Foyevtsova, K.; Valentí, R.; Khomskii, D.I. Na_2IrO_3 as a molecular orbital crystal. *Phys. Rev. Lett.* **2012**, *109*, 197201.
4. Foyevtsova, K.; Jeschke, H.O.; Mazin, I.I.; Khomskii, D.I.; Valentí, R. Ab initio analysis of the tight-binding parameters and magnetic interactions in Na_2IrO_3. *Phys. Rev. B* **2013**, *88*, 035107.
5. Streltsov, S.; Mazin, I.I.; Foyevtsova, K. Localized itinerant electrons and unique magnetic properties of $SrRu_2O_6$. *Phys. Rev. B* **2015**, *92*, 134408.
6. Turco, E.; Bernhardt, A.; Krane, N.; Valenta, L.; Fasel, R.; Juríček, M.; Ruffieux, P. Observation of the Magnetic Ground State of the Two Smallest Triangular Nanographenes. *ACS Au* **2023**, *3*, 1358–1364.
7. Woodward, R.B.; Hoffmann, R. Stereochemistry of Electrocyclic Reactions. *J. Am. Chem. Soc.***1965**, *87*, 395–397.
8. Woodward, R.B.; Hoffmann, R. The Conservation of Orbital Symmetry. *Angew. Chem., Int. Ed.* **1969**, *8*, 781–853.
9. Hoffmann, R.; Woodward, R.B. Conservation of orbital symmetry. *Acc. Chem. Res.* **1968**, *1*, 17–22.
10. Hendon, C.H.; Tiana, D.; Murray, A.T.; Carbery, D.R.; Walsh, A. Helical frontier orbitals of conjugated linear molecules. *Chem. Sci.* **2013**, *4*, 4278–4284.
11. Imamura, A.; Aoki, Y. Helical molecular orbitals around straight-chain polyyne oligomers as models for molecular devices. *Chem. Phys. Lett.* **2013**, *590*, 136–140.
12. Liu, M.; Artyukhov, V.I.; Lee, H.; Xu, F.; Yakobson, B.I. Carbyne from First Principles: Chain of C Atoms, a Nanorod or a Nanorope. *ACS Nano* **2013**, *7*, 10075–10082.
13. Garner, M.H.; Hoffmann, R.; Rettrup, S.; Solomon, G.C. Coarctate and Möbius: The Helical Orbitals of Allene and Other Cumulenes. *ACS Cent. Sci.* **2018**, *4*, 688–700.
14. Garner, M.H.; Jensen, A.; Hyllested, L.O.; Solomon, G.C. Helical orbitals and circular currents in linear carbon wires. *Chem. Sci.* **2019**, *10*, 4598–4608.
15. Orimoto, Y.; Aok, Y.; Imamura, A. Extraction of One-Handed Helical Frontier Orbital in Even [*n*]Cumulenes by Breaking Mirror Images of Right- and Left-Handed Helical Orbitals: Theoretical Study. *J. Phys. Chem. C* **2019**, *123*, 11134–11139.
16. Garner, M.H.; Laplaza, R.; Corminboeuf, C. Helical versus linear Jahn–Teller distortions in allene and spiropentadiene radical cations. *Phys. Chem. Chem. Phys.* **2022**, *24*, 26134–26143.
17. Ozcelik, A.; Aranda, D.; Gil-Guerrero, S.; Pola-Otero, X.A.; Talavera, M.; Wang, L.; Behera, S.K.; Gierschner, J.; Peña-Gallego, Á.; Santoro, F.; Pereira-Cameselle, R.; Alonso-Gómez, J.L. Distinct Helical Molecular Orbitals through Conformational Lock. *Chem. – Eur. J.* **2020**, *26*, 17342–17349.
18. Garner, M.H.; Corminboeuf, C. Correlation between Optical Activity and the Helical Molecular Orbitals of Allene and Cumulenes. *Org. Lett.* **2020**, *22*, 8028–8033.
19. Pinter, P.; Munz, D. Controlling Möbius-Type Helicity and the Excited-State Properties of Cumulenes with Carbenes. *J. Phys. Chem. A* **2020**, *124*, 10100–10110.

20. Garner, M.H.; Corminboeuf, C. Helical electronic transitions of spiroconjugated molecules. *Chem. Commun.* **2021**, *57*, 6408–6411.
21. Bro-Jørgensen, W.; Garner, M.H.; Solomon, G.C. Quantification of the Helicality of Helical Molecular Orbitals. *J. Phys. Chem. A* **2021**, *125*, 8107–8115.
22. Bro-Jørgensen, W.; Solomon, G.C. Understanding Current Density in Molecules Using Molecular Orbitals. *J. Phys. Chem. A* **2023**, *127*, 9003−9012.
23. Gunasekaran, S.; Venkataraman, L. Tight-binding analysis of helical states in carbyne. *J. Chem. Phys.* **2020**, *153*, 124304.
24. Aoki, Y.; Orimoto, Y.; Imamura, A. One-Handed Helical Orbitals in Conjugated Molecules. *ACS Cent. Sci.* **2018**, *4*, 664–665.
25. Gückel, S.; Gluyas, J.B.G.; El-Tarhuni, S.; Sobolev, A.N.; Whiteley, M.W.; Halet, J.-F.; Lapinte, C.; Kaupp, M.; Low, P.J. Iron versus Ruthenium: Clarifying the Electronic Differences between Prototypical Mixed-Valence Organometallic Butadiyndiyl Bridged Molecular Wires. *Organometallics* **2018**, *37*, 1432–1445.
26. Honda, S.; Sugawara, R.; Ishida, S.; Iwamoto, T. A Spiropentasiladiene Radical Cation: Spin and Positive Charge Delocalization across Two Perpendicular Si=Si Bonds and UV–vis–NIR Absorption in the IR-B Region. *J. Am. Chem. Soc.* **2021**, *143*, 2649–2653.
27. Barber, J.S.; Yamano, M.M.; Ramirez, M.; Darzi, E.R.; Knapp, R.R.; Liu, F.; Houk, K.N.; Garg, N.K. Diels−Alder cycloadditions of strained azacyclic allenes. *Nat. Chem.* **2018**, *10*, 953−960.
28. Ramirez, M.; Svatunek, D.; Liu, F.; Garg, N.K.; Houk, K.N. Origins of Endo Selectivity in Diels−Alder Reactions of Cyclic Allene Dienophiles. *Angew. Chem., Int. Ed.* **2021**, *60*, 14989−14997.
29. Baronas, P.; Komskis, R.; Tankelevičiūtė, E.; Adomėnas, P.; Adomėnienė, O.; Juršėnas, S. Helical Molecular Orbitals to Induce Spin–Orbit Coupling in Oligoyne-Bridged Bifluorenes. *J. Phys. Chem. Lett.* **2021**, *12*, 6827–6833.
30. Albert, B.; Hillebrecht, H. Boron: Elementary Challenge for Experimenters and Theoreticians. *Angew. Chem., Int. Ed.* **2009**, 48, 8640−8668.
31. Zhao, D.; He, X.; Li, M.; Wang, B.; Guo, C.; Rong, C.; Chattaraj, P.K.; Liu, S. Density functional theory studies of boron clusters with exotic properties in bonding, aromaticity and reactivity. *Phys. Chem. Chem. Phys.* **2021**, *23*, 24118–24124.
32. Xu, S.; He, C.; Zhao, Y.; Yang, X.; Xu, H. Generalized Octet Rule with Fractional Occupancies for Boron. *J. Am. Chem. Soc.* **2023**, 145, 25003−25009.
33. Zhang, W.; Zhao, Y.; An, X.; Fu, J.; Zhang, J.; Zhao, D.; Liu, S.; Rong, C. Cooperativity and reactivity properties of medium-sized boron clusters: a combined density functional theory and information-theoretic approach study. *Mol. Phys.* **2022**, e2157774.
34. Sergeeva, A.P.; Zubarev, D.Y.; Zhai, H.; Boldyrev, A.I.; Wang, L. A Photoelectron Spectroscopic and Theoretical Study of B_{16}^- and B_{16}^{2-}: An All-Boron Naphthalene. *J. Am. Chem. Soc.* **2008**, *130*, 7244–7246.
35. Kiran, B.; Bulusu, S.; Zhai, H.; Yoo, S.; Zeng, X.; Wang, L. Planar-to-tubular structural transition in boron clusters: B_{20} as the embryo of single-walled boron nanotubes. *Proc. Natl. Acad. Sci. U.S.A.* **2005**, *102*, 961–964.
36. Popov, I.A.; Piazza, Z.A.; Li, W.; Wang, L.; Boldyrev, A.I. A combined photoelectron spectroscopy and *ab initio* study of the quasi-planar B_{24}^- cluster. *J. Chem. Phys.* **2013**, *139*, 144307.
37. Wang, Y.; Zhao, Y.; Li, W.; Jian, T.; Chen, Q.; You, X.; Ou, T.; Zhao, X.; Zhai, H.; Li, S.; Li, J.; Wang, L. Observation and characterization of the smallest borospherene, B_{28}^- and B_{28}. *J. Chem. Phys.* **2016**, *144*, 064307.
38. Von Barth, U.; Hedin, L. A Local Exchange-Correlation Potential for the Spin Polarized Case: I. *J. Phys. C: Solid State Phys.* **1972**, *5*, 1629.
39. Gunnarsson, O.; Lundqvist, B.I. Exchange and Correlation in atoms, molecules and solids by the spin-density-functional formalism. *Phys. Rev. B* **1976**, *13*, 4274–4298.
40. Rajagopal, A.K.; Callaway, J. Inhomogeneous electron gas. *Phys. Rev. B* **1973**, *7*, 1912–1919.
41. Ayers, P.W.; Yang, W. Legendre-transform functionals for spin-density-functional theory. *J. Chem. Phys.* **2006**, *124*, 224108.
42. Galván, M.; Vargas, R. Spin Potential in Kohn–Sham Theory. *J. Phys. Chem.* **1992**, *96*, 1625–1630.
43. Ghanty, T.K.; Ghosh, S.K. Spin-Polarized Generalization of the Concepts of Electronegativity and Hardness and the Description of Chemical Binding. *J. Am. Chem. Soc.* **1994**, *116*, 3943–3948.
44. Garza, J.; Vargas, R.; Cedillo, A.; Galván, M.; Chattaraj, P.K. Comparison between the frozen core and finite differences approximations for the generalized spin-dependent global and local reactivity descriptors in small molecules. *Theor. Chem. Acc.* **2006**, *115*, 257–265
45. Pérez, P.; Chamorro, E.; Ayers, P.W. Universal mathematical identities in density functional theory: Results from three different spin-resolved representations. *J. Chem. Phys.* **2008**, *128*, 204108.
46. Ayers, P.W.; Fias, S.; Heidar-Zadeh, F. The axiomatic approach to chemical concepts. *Comput. Theor. Chem.* **2018**, *1142*, 83-87.
47. Liu, S. Conceptual Density Functional Theory and Some Recent Developments. *Acta Phys.-Chim. Sin.* **2009**, *25*, 590–600.

48. Johnson, P.A.; Bartolotti, L.J.; Ayers, P.W.; Fievez, T.; Geerlings, P. Charge density and chemical reactivity: A unified view from conceptual DFT. In Modern Charge Density Analysis, Gatti, C., Macchi, P. Eds.; Springer, 2012; pp 715-764.
49. Geerlings, P.; Chamorro, E.; Chattaraj, P.K.; De Proft, F.; Gázquez, J.L.; Liu, S.; Morell, C.; Toro-Labbé, A.; Vela, A.; Ayers, P.W. Conceptual density functional theory: status, prospects, issues. *Theor. Chem. Acc.* **2020**, *139*, 36.
50. Jissy, A.K.; Datta, A. What Stabilizes the Li_nP_n Inorganic Double Helices? *J. Phys. Chem. Lett.* **2013**, *4*, 1018–1022.
51. Guo, J.; Feng, L.; Wang, Y.; Jalife, S.; Vásquez-Espinal, A.; Cabellos, J.L.; Pan, S.; Merino, G.; Zhai, H. Coaxial Triple-Layered versus Helical $Be_6B_{11}^-$ Clusters: Dual Structural Fluxionality and Multifold Aromaticity. *Angew. Chem., Int. Ed.* **2017**, 56, 10174-10177.
52. Reber, A.C.; Ugrinov, A.; Sen, A.; Qian, M.; Khanna, S.N. Helical and linear $[K(As_{11})]^{2-}$ chains: Role of solvent on the conformation of chains formed by Zintl anions. *Chem. Phys. Lett.* **2009**, 473, 305–311.
53. Lu, T. Simple, reliable, and universal metrics of molecular planarity. *J. Mol. Model.* **2021**, *27*, 263.
54. Humphrey, W.; Dalke, A.; Schulten, K. VMD: visual molecular dynamics. *J. Mol. Graph.* **1996**, *14*, 33–38.
55. Adamo, C.; Barone, V. Toward reliable density functional methods without adjustable parameters: The PBE0 model. *J. Chem. Phys.* **1999**, *110*, 6158–6169.
56. McLean, A.D.; Chandler, G.S. Contracted Gaussian-basis sets for molecular calculations. 1. 2nd row atoms, *Z*=11-18. *J. Chem. Phys.* **1980**, *72*, 5639–5648.
57. Dennington II, R.D.; Keith, T.A.; Millam, J.M. GaussView 6.0.16, Semichem, Inc. 2000–2016.
58. Ahrens, J.; Geveci, B.; Law, C. ParaView: An End-User Tool for Large Data Visualization. In *Visualization Handbook*. Elesvier, 2005.
59. Jusélius, J.; Sundholm, D.; Gauss, J. Calculation of current densities using gauge-including atomic orbitals. *J. Chem. Phys.* **2004**, *121*, 3952–3963.
60. Fliegl, H.; Taubert, S.; Lehtonen, O.; Sundholm, D. The gauge including magnetically induced current method. *Phys. Chem. Chem. Phys.* **2011**,*13*, 20500–20518.
61. Schleyer, P.v.R.; Maerker, C.; Dansfeld, A.; Jiao, H.; Hommes, N.J.R.v.E. Nucleus-Independent Chemical Shifts: A Simple and Efficient Aromaticity Probe. *J. Am. Chem. Soc.* **1996**, *118*, 6317–6318.
62. Kloda, S.; Kleinpeter, E. *Ab initio* calculation of the anisotropy effect of multiple bonds and the ring current effect of arenes—application in conformational and configurational analysis. *J. Chem. Soc., Perkin Trans.* **2001**, *2*, 1893–1898.
63. Rega, N.; Cossi, M.; Barone, V. Development and validation of reliable quantum mechanical approaches for the study of free radicals in solution. *J. Chem. Phys.* **1996**, *105*, 11060–11067.
64. Barone, V. Electronic, vibrational and environmental effects on the hyperfine coupling constants of nitroside radicals. H_2NO as a case study. *Chem. Phys. Lett.* **1996**, *262*, 201–206.
65. Golding, R.M.; Stubbs, L.C. The Evaluation of the Hyperfine Interaction Tensor Components in Molecular Systems. *Proc. R. Soc. Lond.* A. **1977**, *354*, 223–244.
66. Jensen, F. The Basis Set Convergence of Spin–Spin Coupling Constants Calculated by Density Functional Methods. *J. Chem. Theory Comput.* **2006**, *2*, 1360–1369.
67. Pritchard, B.P.; Altarawy, D.; Didier, B.; Gibson, T.D.; Windus, T.L. A New Basis Set Exchange: An Open, Up-to-date Resource for the Molecular Sciences Community. *J. Chem. Inf. Model.* **2019**, *59*, 4814–4820.
68. Naaman, R.; Paltiel, Y.; Waldeck, D.H. Chiral Molecules and the Electron Spin. *Nat. Rev. Chem.* **2019**, *3*, 250–260.
69. Yang, S.-H.; Naaman, R.; Paltiel, Y.; Parkin, S.S.P. Chiral spintronics. *Nat. Rev. Phys.* **2021**, *3*, 328–343.
70. Liu, Y.; Xiao, J.; Koo, J.; Yan, B. Chirality-driven topological electronic structure of DNA-like materials. *Nat. Mater.* **2021**, *20*, 638–644.
71. Parr, R.G.; Yang, W. *Density Functional Theory of Atoms and Molecules*; Oxford University Press: Oxford, UK, 1989.
72. Teale, A.M.; Helgaker, T.; Savin, A.; Adamo, C.; Aradi, B.; Arbuznikov, A.V.; Ayers, P.W.; Baerends, E.J.; Barone, V.; Calaminici, P.; Cancès, E.; Carter, E.A.; Chattaraj, P.K.; Chermette, H.; Ciofini, I.; Crawford, T.D.; De Proft, F.; Dobson, J.F.; Draxl, C.; Frauenheim, T.; Fromager, E.; Fuentealba, P.; Gagliardi, L.; Galli, G.; Gao, J.; Geerlings, P.; Gidopoulos, N.; Gill, P.M.W.; Gori-Giorgi, P.; Görling, A.; Gould, T.; Grimme, S.; Gritsenko, O.; Jensen, H.J.A.; Johnson, E.R.; Jones, R.O.; Kaupp, M.; Köster, A.M.; Kronik, L.; Krylov, A.I.; Kvaal, S.; Laestadius, A.; Levy, M.; Lewin, M.; Liu, S.; Loos, P.-F.; Maitra, N.T.; Neese, F.; Perdew, J.P.; Pernal, K.; Pernot, P.; Piecuch, P.; Rebolini, E.; Reining, L.; Romaniello, P.; Ruzsinszky, A.; Salahub, D.R.; Scheffler, M.; Schwerdtfeger, P.; Staroverov, V.N.; Sun, J.; Tellgren, E.; Tozer, D.J.; Trickey, S.B.; Ullrich, C.A.; Vela, A.; Vignale, G.; Wesolowski, T.A.; Xu, X.; Yang, W. DFT exchange: sharing perspectives on the workhorse of quantum chemistry and materials science. *Phys. Chem. Chem. Phys.* **2022**, *24*, 28700–28781.
73. Frisch, M.J.; Trucks, G.W.; Schlegel, H.B.; Scuseria, G.E.; Robb, M.A.; Cheeseman, J.R.; Scalmani, G.; Barone, V.; Petersson, G.A.; Nakatsuji, H.; *et al*. Gaussian 16 Revision C.01; Gaussian Inc.: Wallingford, CT, USA, 2016.

 doi:10.20944/preprints202402.0801.v1

74. Lee, T.J.; Taylor, P.R. A diagnostic for determining the quality of single-reference electron correlation methods. *Int. J. Qunantum Chem.* **1989**, *36*, 199–207.
75. London, F. The quantic theory of inter-atomic currents in aromatic combinations. *J. Phys. Radium* **1937**, *8*, 397–409.
76. McWeeny, R. Perturbation Theory for Fock-Dirac Density Matrix. *Phys. Rev.* **1962**, *126*, 1028–1034.
77. Ditchfield, R. Self-consistent perturbation theory of diamagnetism. 1. Gauge-invariant LCAO method for N.M.R. chemical shifts. *Mol. Phys.* **1974**, *27*, 789–807.
78. Wolinski, K.; Hinton, J.F.; Pulay, P. A Comparison of Models for Calculating Nuclear Magnetic Resonance Shielding Tensors. *J. Am. Chem. Soc.* **1990**, *112*, 8251–8260.
79. Cheeseman, J.R.; Trucks, G.W.; Keith, T.A.; Frisch, M.J. A comparison of models for calculating nuclear magnetic resonance shielding tensors. *J. Chem. Phys.* **1996**, *104*, 5497–5509.
80. Lu, T.; Chen, F. Multiwfn: A multifunctional wavefunction analyzer. *J. Comput. Chem.* **2011**, *33*, 580–592.